Temperature Effects on Damage Mechanisms of Hybrid Metal – Composite Bolted Joints Using SHM Testing Method

Calin-Dumitru COMAN*,[1], Ion DIMA[1], Stefan HOTHAZIE[1], George PELIN[1], Tiberiu SALAORU[1]

*Corresponding author
*,[1]INCAS – National Institute for Aerospace Research "Elie Carafoli",
Department of Structures and Materials,
B-dul Iuliu Maniu 220, Bucharest, 061126, Romania,
coman.calin@incas.ro*, dima.ion@incas.ro, hothazie.stefan@incas.ro,
pelin.george@incas.ro, salaoru.tiberiu@incas.ro

DOI: 10.13111/2066-8201.2019.11.1.5

Received: 15 October 2018/ Accepted: 03 January 2019/ Published: March 2019

Abstract: *This paper presents the quasi-static thermo-mechanical loading effects on the progressive damage mechanisms and failure modes of the single-bolt, single-shear, hybrid metal-composite, bolted joints in aerospace applications. A three-dimensional finite element method (FEM) technique was used to model the countersunk head bolted joint in details, including geometric and frictional based contact full nonlinearities and using commercial software PATRAN as pre/post-processor. The progressive damage analysis (PDA) in laminated (CFRP/ vinyl ester epoxy) composite material including nonlinear shear behavior, Hashin-type failure criteria and strain-based continuous degradation rules for different values of temperatures was made using SOL 400 NASTRAN solver. In order to validate the numerical results and close investigation of the fracture mechanisms for metal-composite bolted joints by determining ultimate failure loads, experiments were conducted in temperature controlled chamber using SHM (Structural Health Monitoring) technique. The results show that the thermal effects are not negligible on failure mechanism in hybrid aluminum-CFRP bolted joints having strong different thermal expansion coefficients. The complex 3D FEM model using advanced linear continuum solid-shell elements proved computational efficiency and ability to accurately predict the various failure modes as bearing and shear-shear out, including the temperature effects on the failure propagation and damage mechanism of hybrid metal-composite bolted joints.*

Key Words: *Progressive Damage, Temperature, Failure, SHM*

1. INTRODUCTION

The aerospace industry became the most common application field for fiber-reinforced polymer matrix composites (PMCs) due to their lightweight properties [1]. These structural components are often assembled in conjunction with metal parts using mechanically fastened joints resulting in hybrid metal-composite joints which determinate some challenging problems for mechanical engineers. The poor designed hybrid joints are not only a source of failure, but could lead to a reduction in durability and reliability of the whole structure. So

far, the researchers have studied the failure of composite bolted joints using a method that combines continuum damage mechanics (CDM) [2] with finite element analysis (FEA). In the CDM case, the local damage onset appears at a low value of applied load and damage accumulation is developed with increasing load according to damage propagation lows, which makes the method accurate and able to predict various failure modes. The major disadvantage of the CDM models is the huge amount of test data required for model calibrations. The progressive damage analysis (PDA) in composite materials, which is based on the stress-strain failure criterion, showed that the material orthotropic properties reduction due to damage initiation is essential for the stress field analysis [3-7]. A lot of PDA models in research field [8-11] incorporated shear nonlinearity, Hashin type failure criterion and constant elastic properties degradation low for orthotropic materials, which makes the method quite easy to implement and computational efficient. Because these properties degradation models have used constant factors to reduce elastic properties due to increased damage, the models were not able to predict the bearing final failure.

Models containing continuous degradation rules started to appear in the literature [12], [13] to improve the numeric algorithm converge and to obtain a smoother loading-displacement curve. A major lack of these models is that they have focused only on a few types of failure mode and do not refer to various joint failure modes. The composite progressive damage behavior is a complex nonlinear phenomenon and in conjunction with geometric and contact nonlinearities can lead to divergence of the finite element method (FEM) analysis, mostly in implicit numerical algorithms which implies that a much effort is spent to obtain a converged solution toward to ultimate global structure failure.

The composite materials can withstand with increasing temperature up to 300^0C, having good properties in high pressure, low thermal expansion coefficient, high thermal conductivity, high thermal shock resistance and low depression [14]. The difficulties arising from the use of composite materials on structural failure problems are that these materials have anisotropic mechanical properties, brittle and low inter-laminar strength [15].

This study describes and develops a progressive damage analysis using an adequate material model for composite plate that can predict the thermal effects on loading structural behavior and failure modes of hybrid metal-composite bolted joints. The analysis takes into account all the nonlinearities phenomena involved in load transition trough the joint as geometric nonlinearity which imply large deformations, friction based full nonlinear contact and material nonlinearities due to shear deformations of the lamina, Hashin-type failure criterion and strain-based continuous degradation rules implemented, using an user subroutine in commercial Nastran SOL 400 solver. A series of experiments were conducted in order to validate the FE model and PDA results involving the influence of temperature on the failure modes of the hybrid-metal composite joints. The experimental and numerical results fit quite accurate for the influence of temperature on the stiffness and failure load of hybrid metal-composite bolted joints.

2 PROBLEM DESCRIPTION

2.1 Joint geometry description

Single-lap joints (SLJ) with hexagonal head bolts were manufactured using both metal and composite materials for the adherents. The geometry of the joint model is presented in Fig.1. The geometry design was chosen in accordance with ASTM standard [16] to induce bearing failure. The in-plane dimensions of the each plate are identical, as follows: 150 mm length

and 50 mm width. The thicknesses are different, 4 mm for the metal plate and 2 mm for the laminated plate. Hexagonal head stainless steel bolts with nominal diameter of 5 mm with 0.5 N m torque level applied in dry conditions.

The composite plate was made from carbon-epoxy pre-pregs with fiber volume fraction 32 %. The symmetric stacking sequence is represented by $[0/90]_{3s}$ using 0.33 mm thickness unidirectional lamina, with the elastic properties, presented in Table 1. The metal plate was manufactured from aluminum alloy AA 7075T6 and the bolts, nuts and washers were made from stainless steel A2-70 with the elastic properties presented in Table 1 as well. A group of five specimens were prepared for the thermal effects study on the failure mechanisms in the laminated plate.

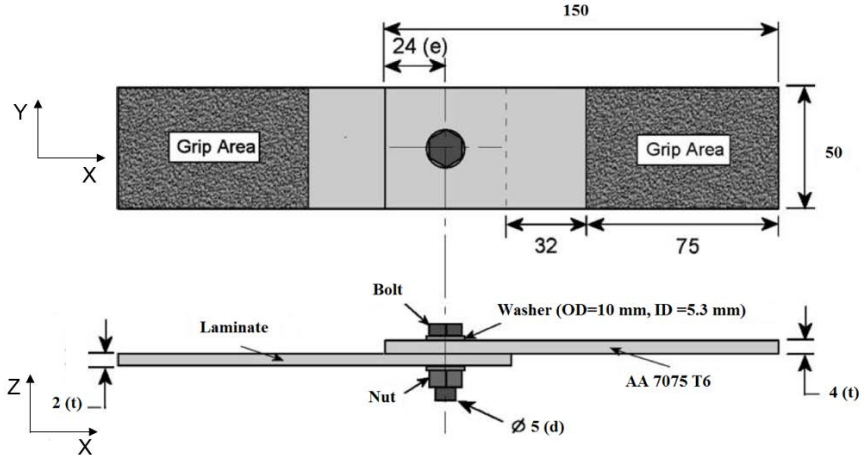

Figure 1. Countersunk joint geometry, dimensions in mm.

The mechanical properties of all the materials used are presented in Table 1, where the lamina principal directions (1, 2, 3) are the same with global coordinate axis shown in Fig. 1. The unidirectional elastic properties presented in Table 1 were obtained using ASTM, [16], [17] standards tests on the unidirectional laminated coupons. Regarding the thermal expansion coefficient of the composite plate, a micro-analysis method has been used to calculate this coefficient at lamina level using the thermal coefficients of the fibers and matrix. According to [18] and [19] we have α_{fiber}= - 0.41 ($10^{-6}/\,^{o}C$), α_{matrix}= 40 ($10^{-6}/\,^{o}C$). Using these values and equation (1) it can be obtained [20]:

$$\alpha_{11}=\frac{E_{fiber}\cdot V_{fiber}\cdot\alpha_{fiber}+E_{matrix}\cdot(1-V_{fiber})\cdot\alpha_{matrix}}{E_{11}}=2\ (10^{-6}/^{o}C) \tag{1}$$

$$\alpha_{22}=\alpha_{33}=44\ (10^{-6}/^{o}C) \tag{2}$$

Table 1. Material Properties

Property	Lamina	AA 7075T6 Ref. [21]	A2-70 Ref. [21]
Longitudinal modulus E_{11} (MPa)	34433	71016	206000
Transversal modulus E_{22} (MPa)	3610		
Through-thickness modulus, E_{33} (MPa)	3610		
Shear modulus G_{12} (MPa)	2421	26890	75842
Shear modulus G_{23} (MPa)	2421		
Shear modulus G_{13} (MPa)	1561		
Poisson coefficient υ_{12}	0.36	0.33	0.36
Poisson coefficient υ_{23}	0.45		

Poisson coefficient υ_{13}	0.35		
Longitudinal CTE α (10^{-6}/ºC)	2	24	18
Transversal CTE α (10^{-6}/ºC)	44		
Through-thickness CTE α (10^{-6}/ºC)	44		
Longitudinal tensile strength $\sigma_{11,\,max}^{T}$, (MPa)	253		
Longitudinal compression strength $\sigma_{11,\,max}^{C}$, (MPa)	230		
Transversal compression strength $\sigma_{22,\,max}^{C}$, (MPa)	74		
In plane shear strength τ_{12}^{max}, (MPa)	25		
Out plane shear strength τ_{23}^{max}, (MPa)	37		
Out plane shear strength τ_{13}^{max}, (MPa)	37		

After joints installation set-up, the specimens were gripped in the 30 kN Instron 3367 universal test machine connected to a temperature controlled chamber. The used chamber is Instron SFL 3119-400 series, the temperature controlled ranges between (-70/+250 ºC) and the frozen agent is CO_2 liquid.

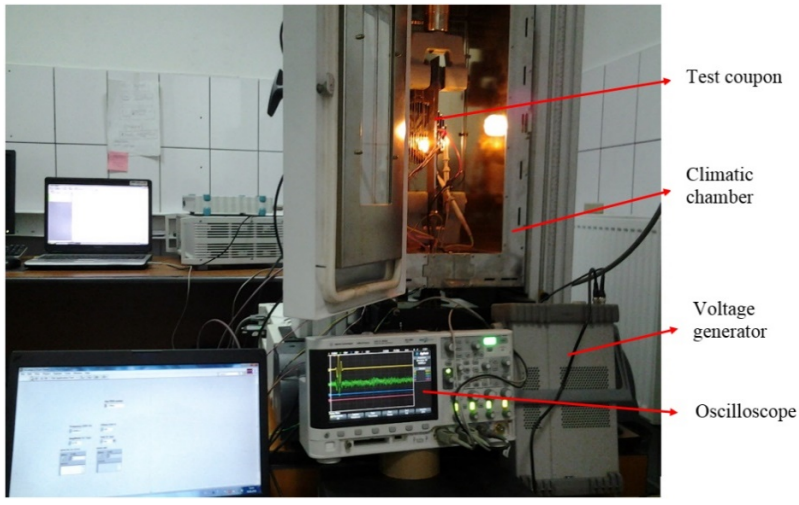

Figure 2. Experimental workbench

The bearing tests were conducted in accordance with ASTM standard [16] and the specimens were loaded in displacement controlled at 0.3 mm/min until the ultimate failure at temperatures T= +50ºC and T= -50ºC.

2.2 Numerical model description

A tridimensional finite element model, using linear eight nodes brick elements, was developed in commercial software MSC Patran for the joint model, shown in Fig. 3. Each separate part was modeled: the metal and composite plates, the washers and a combined bolt-nut part. The plates were meshed with high radial mesh density around the hole, where high strain gradients exists.

In order to avoid rigid body motions, light springs were attached to the components not fully constrained, such as the bolt, washers and laminate plate. For simulating the bolt pre-load due to the torque level, a 330 N axial force was applied in the bolt shank using Bolt Preload Module in Patran.

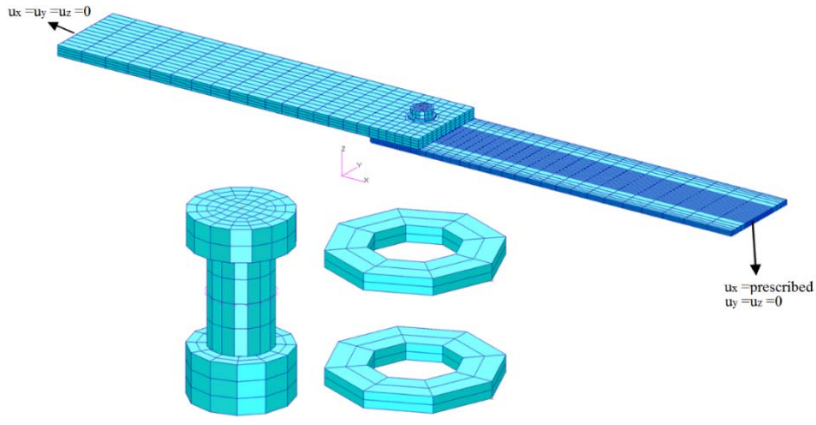

Figure 3. 3D finite element model

Regarding the clamping of the joint in the test machine, the boundary conditions imposed on the model are presented in Fig.3. They represent the fixing of all the translations only on top and bottom surfaces of the metal plate leftmost end and the blocking only of the translations on Y and Z directions imposing a prescribed displacement on X direction at the composite plate rightmost end. The laminated plate is modelled with continuum solid-shell special elements available in MSC Nastran 2012. These special solid elements have bending properties like shells and one integrating point per element. The finite element model has six elements per laminate thickness plate, with one solid-shell element per each ply; thus, stress in each ply can be determined and the correct bending-twisting coupling is obtained. In the 3D model, the contact between the bolt and the surface of the hole is achieved by the direct method of the constraints explained in the following. The method requires the definition of contact bodies that can come into contact. The bodies in contact may be whole physical bodies (laminated plates, bolt, washer), but it has been shown [22] that it is more efficient to consider sets of elements of these physical bodies in contact, as shown in Fig. 4, because the number of checks for contact between bodies at each iteration of the solution is reduced.

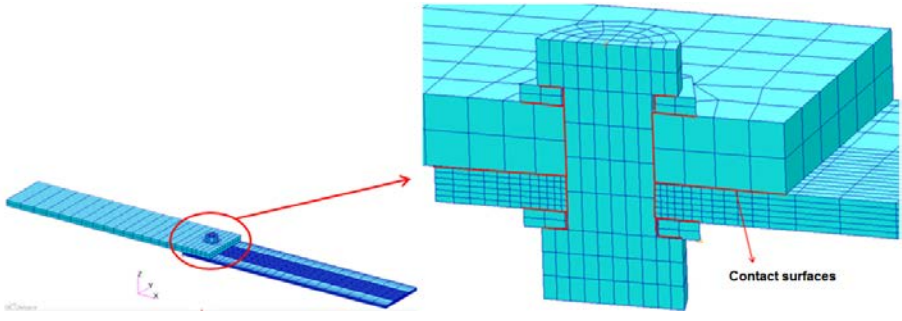

Figure 4. Contact elements in 3D model

A specific tolerance is used to determine if a node penetrates the nearest segment and then it is considered to be in contact with that segment; if so, it is moved to the segment and constrained to stay on it. If the node penetrates the tolerated contact area, the solution is resumed and a new node position is calculated by checking if it is in the contact tolerated area. If the tolerance is too small then the iteration time of the solution and the determination of the node position in the tolerated zone will be very long and considerable hardware resources will be required, but too big tolerance will lead to a premature and unrealistic determination of the contact between the two bodies.

The default contact tolerance value in PATRAN is the twentieth part of the smallest side of the smallest element. In PATRAN, there is the possibility of defining contact as "single-sided" or "double-sided", the contact between the bodies is made in one sense or in both senses and the order in which the two bodies are defined in contact is important. In the present paper, only the "single-sided" contact is used, since the "double-sided" variant can lead to cracks at the contact interface and the joining component with the finer (stiffer) mesh has to be defined the first (slave) in the process of defining the contact; the component with a coarser mesh must be defined the second (master).

This order for defining the bodies in contact has a direct implication on the restrictions imposed on the FEM model of the joint. Another step in defining the nonlinear contact phenomena is the choice between the analytical contact and the discreet contact, which will be briefly described below. When a node on a solid reaches the contact segment on the other solid, the node is constraint on this segment along the normal to this segment. In the case of discrete contact for normal detection, the linear representation with the finite elements of the contact surface is used, which leads to the calculation of the normal of each element.

If the surface is not planar, when the node reaches the contact segment on the surface of the other solid in contact, being in the tolerated contact area, it is shifted and constrained on the contact segment, making possible the movement and constraint process; because the surface has a curve, the node blocks between 2 different normal elements due to the discontinuity of the normal elements.

This impediment has an adverse effect on the quality of the results as observed by McCarthy et al. [22] in their work on single bolt joint, single shear of composite materials.

In the case of analytical contact, a smooth Coons surface is constructed through the nodes of the solid contact segment, and then this analytical surface is used to calculate the continuous normal at the contact surface between the two solids, thus solving the problem of blocking the node between two surfaces normal due to the discontinuity of the contact surfaces. This method leads to a better representation of the joint geometry, especially its deformation; the accuracy of the numerical results is far superior to the technique of discrete contact [22].

3 TEMPERATURE EFFECTS ON JOINT STIFFNESS

3.1 Model validation

In this section, the test results are compared to the results of the three-dimensional finite element model described in the previous chapter. Strains at selected points on the surface of the laminated plate are used to check the accuracy of the finite element model. The joints were strain gauged and loaded in tensile to a level that prevents any damage of the composite plate (1.2 kN) at T = 50^{o}C. Fig. 5 presents the locations of the strain gauges with 3 mm length; all gauges are aligned to the loading direction and located on the bottom surface of the laminate plate, except the gauge number 2 which is located in the shear plane on the top surface. The numerical and experimental results for strains are shown in Table 2 and Fig. 6. Table 2 clearly shows that strain gauges 1 and 2 indicate a joint bending despite the fact that the loading is a tensile load. The readings for gauges 3 and 4 are quite different indicating a twisting effect of the joint along the longitudinal axis which is the loading axis. From Table 2, it can be concluded that the model predicted satisfactory the linear behavior of the joint and can be used in the following temperature parametric study for the linear response of the hybrid metal-composite joint.

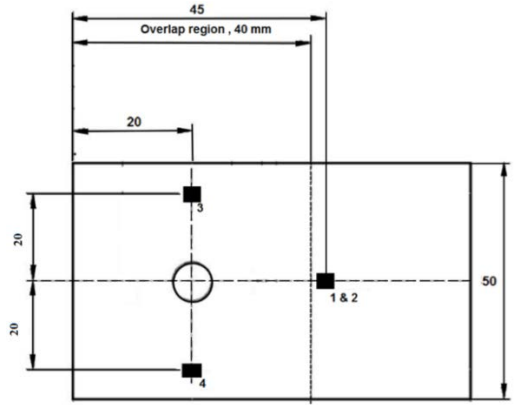

Figure 5. Strain gauge locations, all dimensions are in mm

Table 2. Experimental and numerical strain readings, 1.2 kN applied load

Gauge number	Experimental strain (μm/m)	Numerical strain (μm/m)
1	376	380
2	-1300	-1252
3	357	329
4	339	315

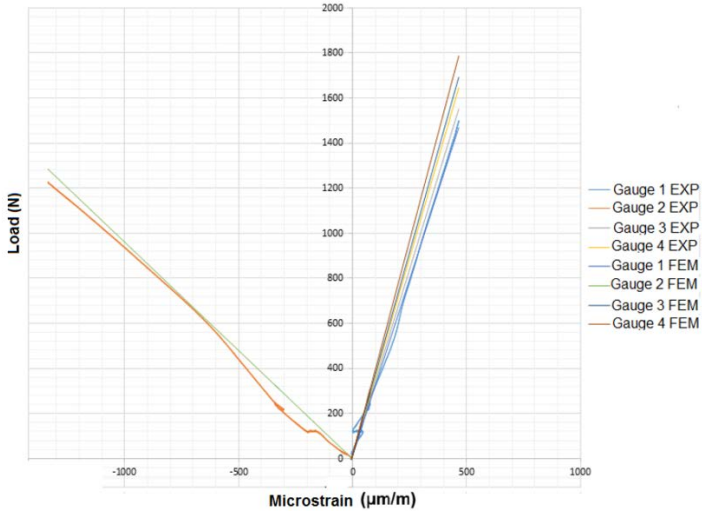

Figure 6. Experimental and numerical surface strains

3.2 Joint stiffness

The effects of the temperature on the joint axial stiffness are presented in this subchapter. The tests setup is shown in Table 3 for single-bolt, single-lap, metal-composite joints. From the experimental results it was observed that the load-displacement curves are approximately linear between applied forces 0.2 - 1 kN in the experiment and 0.1-1.5 kN in the simulation for temperature T = +50 ^{0}C, but 0.1-3.3 kN in the experiment and 0.2-3.5 kN in the simulation for temperature T = - 50 ^{0}C; therefore, the stiffness of the joint is determined for these load ranges. The joint load was obtained directly from the testing machine; the displacement was measured with optical extensometers. The load-displacement curves for the two temperature values are presented in Fig. 7.

Table 3. Experiment setup

Test number	Number of specimens	Torque level (Nm)	Temperature (ºC)
1	5	0.5	-50
2	5	0.5	+50

The first nonlinear segments on the experimental curves from Fig. 7 are explained by the friction between the plates. For a low level of the applied load, the forces are transmitted through the friction and the plates do not move relatively, so the shank of the bolt do not bear the hole surface due to the initial clearance fit in the joint. The joint under investigation has a close tolerance clearance of 48 µm according to f7H10 standard fit tolerances. As long as F > µP, where F is the applied joint load, µ=0.235 is the frictional coefficient between aluminum AA 7075 and CFRP plates as Schon [23] measured experimentally; P = 330 N is the plates clamping force due to preload, the friction is overcomes and the bolt shank bears the hole surface. From now on, the joint is elastically deformed, the axial stiffness is fully developed and can be determined. The experimental and numerical axial stiffness, calculated as the slope of the approximately linear portions of the load-displacement curves, is presented in Table 4. From Table 4 and Fig.7, it can be observed that the temperature reduces the stiffness of the hybrid metal-composite joint both in the experiment and simulation results, due to the fact that the matrix is plasticized under high temperature and due to low volume ratio of carbon within the composite material (32 %).

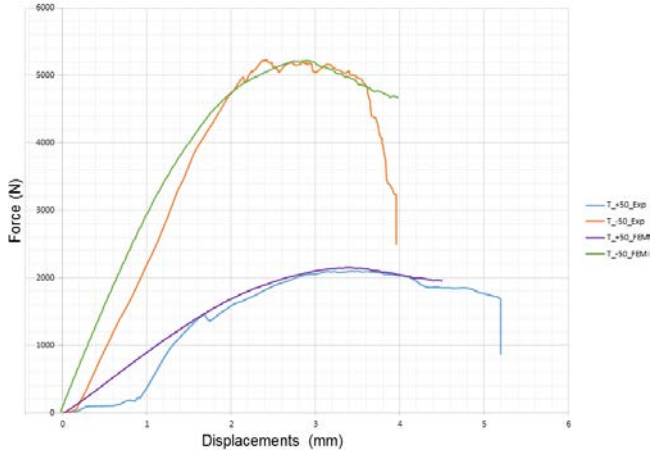

Figure 7. Load-displacement curves

Table 4. Thermal effects on axial stiffness

Stiffness (kN/mm)		Temperature (^{0}C)
Experiment	Simulation	
2.67	2.89	-50
2.11	2.31	+50

4. TEMPERATURE EFFECTS ON JOINT FAILURE

4.1 Lamina nonlinear shear deformation

In order to better understand the nonlinear structural behavior and failure mechanisms in the composite laminated plate of the joint, the load-displacement curves for the two temperature values are presented in Fig. 7.

The simulation must take into account the two most important nonlinear mechanisms: lamina nonlinear shear deformations and stiffness reduction due to damage accumulation at lamina level. These two nonlinearities are taken into account using an external user-defined subroutine named USER_MAT, edited in FORTAN language. USER_MAT calls the modified predefined Nastran material user-defined subroutines UMAT and UPROGFAIL, in order to implement the material nonlinearities specified above. Hahn and Tsai developed [24] the in plane nonlinear shear lamina constitutive model using high order elasticity theory:

$$\gamma_{12} = \frac{\tau_{12}}{G_{12}} + \beta \cdot \tau_{12}^3 \tag{3}$$

where β is a material parameter that can be determined by experiments only.

Fig. 8 presents the experimental curve of the shear deformation γ_{12} as a function of the shear stress τ_{12} obtained using off-axis tension tests on unidirectional laminates. From the Fig. 8, by polynomial interpolation, the coefficient β = 0.635 was obtained for this type of lamina used in the study. This constitutive relation can be implemented in USER_MAT user subroutine as it is described in [25]:

$$\tau_{12}^{(t+\Delta t)} = \frac{1+2\cdot\beta\cdot(\tau_{12}^t)^3\cdot(\gamma_{12}^t)^{-1}}{1+3\cdot\beta\cdot G_{12}{}^0\cdot(\tau_{12}^{(t)})^2}\cdot G_{12}{}^0\cdot\gamma_{12}^{t+\Delta t} \tag{4}$$

The orthotropic stress-strain constitutive relationship is given by equations (5) and (6), according to [20]:

$$\begin{bmatrix}\sigma_{11}^{t+\Delta t}\\ \sigma_{22}^{t+\Delta t}\\ \sigma_{33}^{t+\Delta t}\end{bmatrix} = \begin{bmatrix} E_{11}B(1-\vartheta_{23}\vartheta_{32}) & E_{22}B(\vartheta_{12}-\vartheta_{13}\vartheta_{32}) & E_{33}B(\vartheta_{13}-\vartheta_{12}\vartheta_{23})\\ E_{22}B(\vartheta_{12}-\vartheta_{13}\vartheta_{32}) & E_{22}B(1-\vartheta_{13}\vartheta_{31}) & E_{22}B(\vartheta_{32}-\vartheta_{12}\vartheta_{31})\\ E_{33}B(\vartheta_{13}-\vartheta_{12}\vartheta_{23}) & E_{22}B(\vartheta_{32}-\vartheta_{12}\vartheta_{31}) & E_{33}B(1-\vartheta_{12}\vartheta_{21})\end{bmatrix} \times \begin{bmatrix}\varepsilon_{11}^{t+\Delta t}\\ \varepsilon_{22}^{t+\Delta t}\\ \varepsilon_{33}^{t+\Delta t}\end{bmatrix} \tag{5}$$

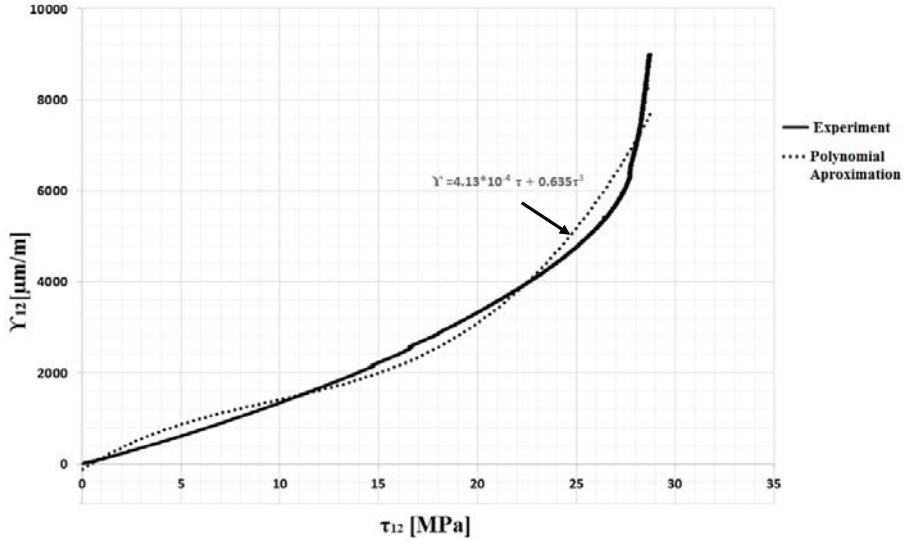

Figure 8. Nonlinear shear–strain experimental curve

$$\begin{bmatrix}\tau_{12}^{t+\Delta t}\\ \tau_{23}^{t+\Delta t}\\ \tau_{31}^{t+\Delta t}\end{bmatrix}=\begin{bmatrix}Rel.(10) & 0 & 0\\ 0 & G_{23} & 0\\ 0 & 0 & G_{31}\end{bmatrix}\times\begin{bmatrix}\gamma_{12}^{t+\Delta t}\\ \gamma_{23}^{t+\Delta t}\\ \gamma_{31}^{t+\Delta t}\end{bmatrix} \tag{6}$$

where:

$$B=\frac{1}{1-\vartheta_{12}\vartheta_{21}-\vartheta_{23}\vartheta_{32}-\vartheta_{13}\vartheta_{31}-2\cdot\vartheta_{21}\vartheta_{32}\vartheta_{13}} \tag{7}$$

$$\tau_{12}^{t+\Delta t}=\begin{cases}\dfrac{1+2\cdot\beta\cdot(\tau_{12}^{t})^{3}\cdot(\gamma_{12}^{t})^{-1}}{1+3\cdot\beta\cdot G_{12}{}^{0}\cdot(\tau_{12}^{t})^{2}}\cdot G_{12}{}^{0}\cdot\gamma_{12}^{(t+\Delta t)}, & FI=0\\ G_{12}{}^{t+\Delta t}\cdot\gamma_{12}^{t+\Delta t}, & FI\geq 1 \text{ and } G_{12}{}^{t+\Delta t}\cdot\gamma_{12}^{t+\Delta t}<\tau_{12}^{init}\\ \tau_{12}^{init}, & FI\geq 1 \text{ and } G_{12}{}^{t+\Delta t}\cdot\gamma_{12}^{t+\Delta t}\geq\tau_{12}^{init}\end{cases} \tag{8}$$

$$FI=max\,(FI_1,FI_2) \tag{9}$$

In relation (8), $G_{12}{}^{0}$ is the initial in-plane shear modulus which is reduced according to degradation rules specified in relation (13), when fiber compression-shear failure happened, FI_1 and FI_2 are defined in relations (10), (11). The shear stress $\tau_{12}{}^{init}$ is a threshold used to avoid any over-estimation of the shear stress after any failure that can reduce the shear modulus G_{12}.

4.2 Failure criteria and continuous degradation rules

The most dominant micro-failure modes for bearing joints are matrix compression and fiber shear-compression failures; therefore, they are given a great deal of attention in this joint failure study. For the PDA of the laminated plate around the hole, Hashin [26] failure criteria is used and the failure indexes are calculated using formula (10) for matrix compression and formula (11) for matrix-fiber shear failure:

$$FI_1=\left[\left(\frac{\sigma_{22,\,max}^{C}}{2\cdot\tau_{23}^{max}}\right)^{2}-1\right]\cdot\frac{\sigma_2+\sigma_3}{\sigma_{22,\,max}^{C}}+\frac{(\sigma_2+\sigma_3)^2}{4\cdot(\tau_{23}^{max})^{2}}-\frac{\sigma_2\cdot\sigma_3}{(\tau_{23}^{max})^{2}}+\left(\frac{\tau_{12}}{\tau_{12}^{max}}\right)^{2}+\left(\frac{\tau_{13}}{\tau_{13}^{max}}\right)^{2}+\left(\frac{\tau_{23}}{\tau_{23}^{max}}\right)^{2} \tag{10}$$

$$FI_2=\left(\frac{\sigma_1}{\sigma_{11.\,max}^{C}}\right)^{2}+\left(\frac{\tau_{12}}{\tau_{12}^{max}}\right)^{2}+\left(\frac{\tau_{13}}{\tau_{13}^{max}}\right)^{2} \tag{11}$$

4.2.1 Continuous degradation rules for elastic modulus

A strain based degradation rule is proposed for reduction of E_{ii} (i=1.. 3) as described in [27, 28]. The fiber or matrix failure initiate at a user-defined failure strain $\varepsilon_{ii}{}^{init}$ and PDA stiffness reductions are performed using relation (12):

$$E_{ii}^{t+\Delta t}=\begin{cases}E_{ii}^{0}\cdot\left(1-d_i\cdot\dfrac{\varepsilon_{ii}^{t+\Delta t}-\varepsilon_{ii}^{init}}{\Delta\varepsilon_{ii}}\right), & \varepsilon_{ii}^{init}\leq\varepsilon_{ii}^{t+\Delta t}<\varepsilon_{ii}^{init}+\Delta\varepsilon_{ii}\\ E_{ii}^{0}\cdot(1-d_i)\dfrac{\varepsilon_{ii}^{init}+\Delta\varepsilon_{ii}}{\varepsilon_{ii}^{t+\Delta t}}, & \varepsilon_{ii}^{t+\Delta t}\geq\varepsilon_{ii}^{init}+\Delta\varepsilon_{ii}\end{cases} \tag{12}$$

where $E_{ii}{}^{0}$ is the initial modulus of elasticity from Table 1 for lamina principal directions, $\Delta\varepsilon_{ii}$ is a strain step, user-defined to ensure a smooth reduction of the properties upon failure and d_i is the reduction factor. Initial failure strain and corresponding stress $\varepsilon_{ii}{}^{init}$, $\sigma_{ii}{}^{init}$ are determined by simulation for FI=1 according to relation (9).

4.2.2 Continuous degradation rules for shear modulus

The in-plane shear modulus G_{12} is continuous reduced using the highest in-plane shear strain $\gamma_{ij}^{t+\Delta t}$ for $FI > 1$, according to:

$$G_{ij} = G_{ij}^{0}\left(0.1 + 0.9 \cdot \frac{\gamma_{ij}^{init}}{\gamma_{ij}^{t+\Delta t}}\right), i \neq j = 1..3 \tag{13}$$

The reduction parameters for E_{ii} (i=1..3) are presented in Table 5 obtained after several parameter tuning iterations.

Table 5. Degradation parameters for elastic moduli

Failure mode	d_i	$\Delta\varepsilon_{ii}$
Fiber shear-compression (i=1)	0.45	0.01
Matrix compression (i=2,3)	0.57	0.01

4.2.3 Poisson's coefficient reduction

In [22] a continuous reduction of the Poisson's ratio is proposed in order to comply with the elastic stability of the orthotropic materials:

$$\vartheta_{12}=\vartheta_{12}^{0}\cdot\sqrt{\frac{E_1E_2^0}{E_2E_1^0}}\ ,\ \vartheta_{13}=\vartheta_{13}^{0}\cdot\sqrt{\frac{E_1E_3^0}{E_3E_1^0}}\ ,\ \vartheta_{23}=\vartheta_{23}^{0}\cdot\sqrt{\frac{E_2E_3^0}{E_3E_2^0}} \tag{14}$$

4.3 Results

The comparison between the experimental and numerical results in terms of the thermal effects on damage initiation and progressive failure mechanism are presented in the following. Load-displacement curves for each temperature value are presented in Figs. 9 and 10.

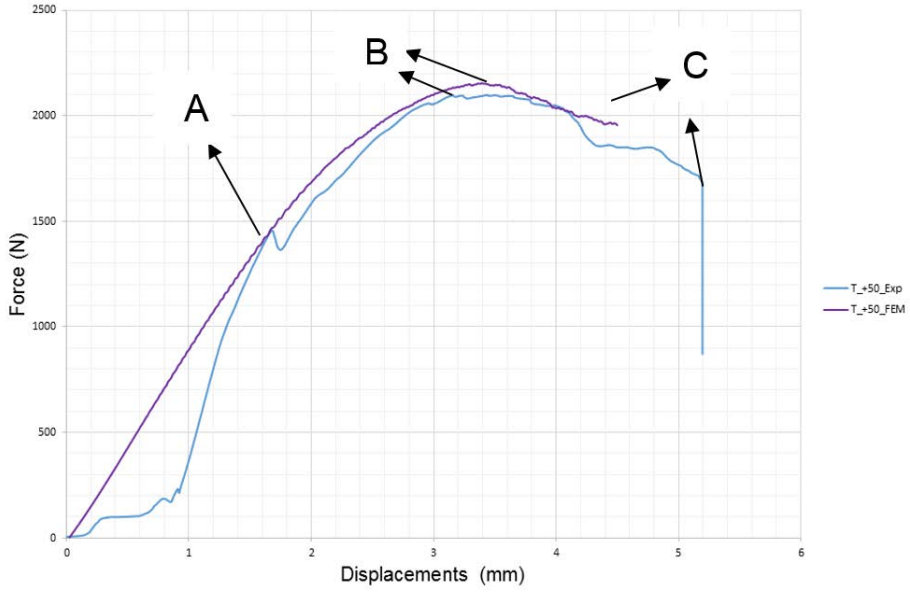

Figure 9. Load-displacement behavior, T=+50 °C

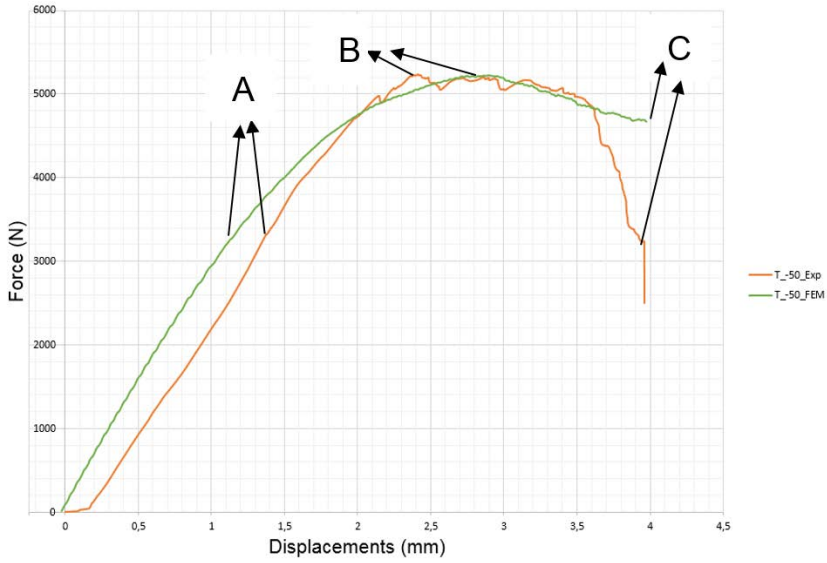

Figure10. Load-displacement behavior, T = -50 ºC

From the Figs. 9 and 10 it can be seen that the temperature has significantly increased the limit (deviation from linearity) and ultimate (maximum) loads (F_{limit}, F_{ult}). In point A on the characteristic load-curves, the fiber and matrix compression damage onset around the hole is evident according to Fig. 11. At the beginning of the test, the structural response of the joint is dominated by the friction between the plate up to 0.5 mm for T = +50 º C and 0.1 mm for T = -50 º C. From the end of the friction stage up to point A, the structural behavior of the hybrid joint is almost linear with small fluctuations which represent small matrix compression damages, but this do not affect the overall joint stiffness. Moving from point A to point B on the load-displacement curves, the damage accumulation is increasing and dominated by matrix tension/compression, fiber-matrix shear as can be seen in Fig. 11 for temperature T= -50 ºC and Fig. 13 for T= +50 ºC, while the joint is loosening its stiffness gradually. Point B defines the ultimate failure load of the joint. The shear-out failure starts to develop from point B due to through thickness shear cracks propagation as illustrated in Fig. 11 up to final structural failure of the joint depicted in Fig. 12 and 14.

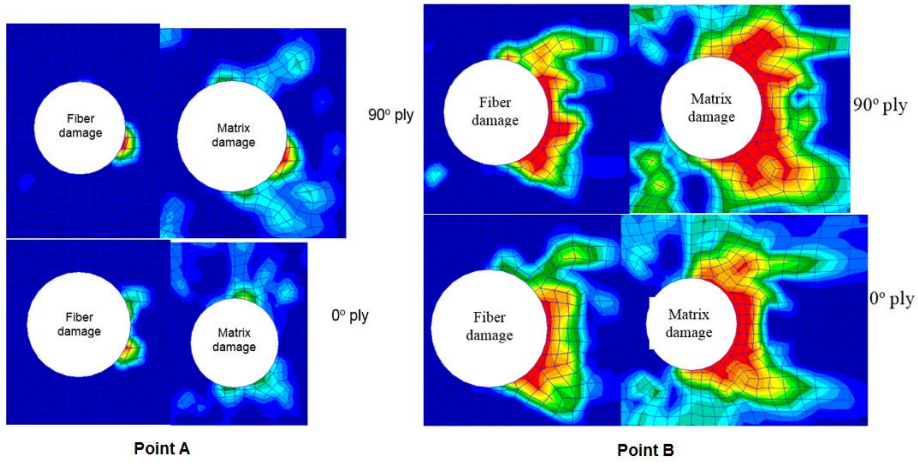

Figure 11. Progressive damage, points A and B, T= - 50 ºC

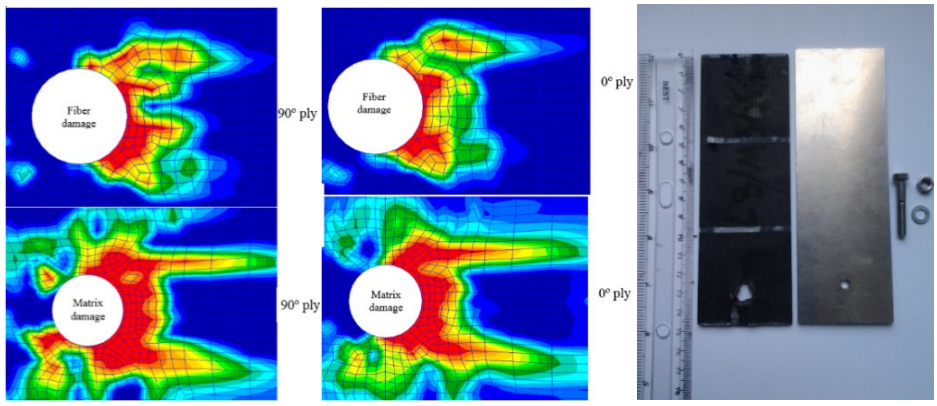

Figure 12. Catastrophic failure, point C, T= - 50 ºC

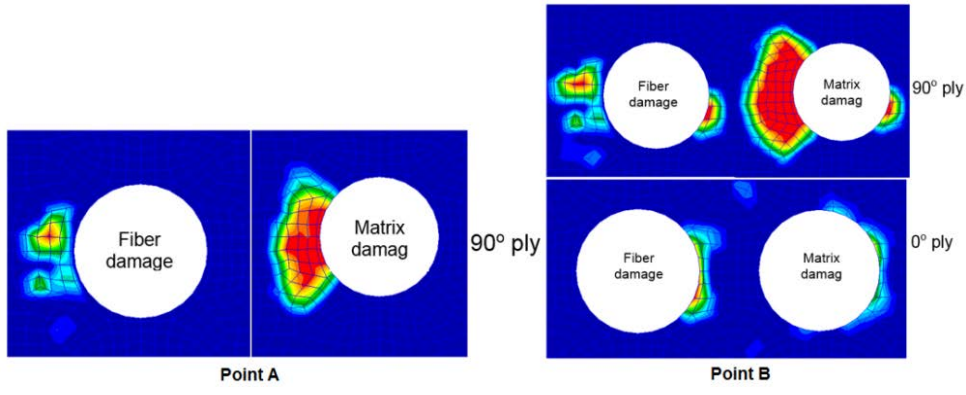

Figure 13. Progressive damage, points A and B, T= + 50 ºC

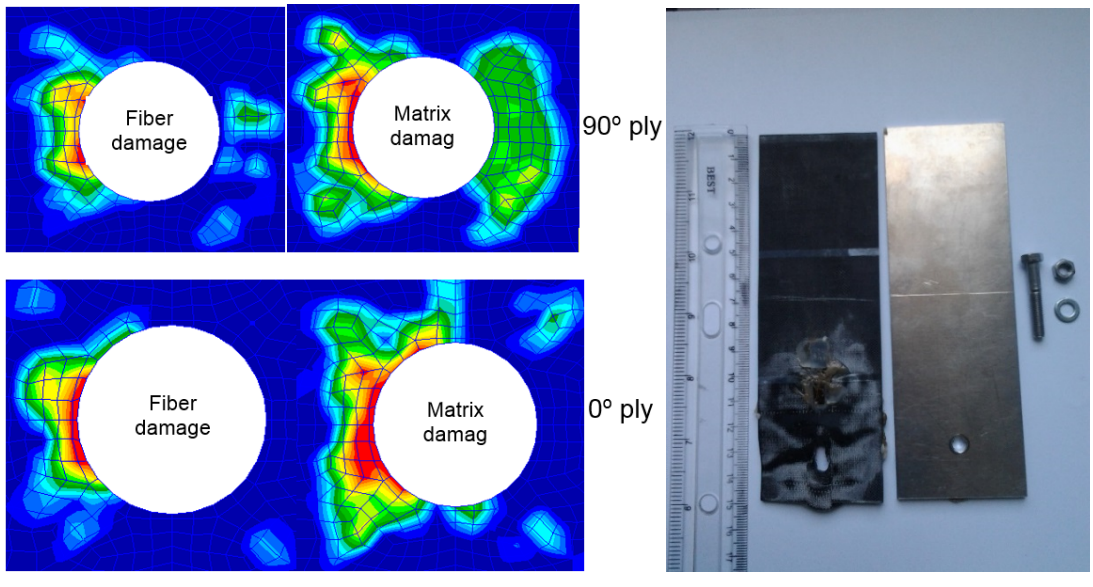

Figure 14. Catastrophic failure, point C, T= + 50 ºC

A summary of the thermal effects on the progressive failure of the countersunk metal-composite hybrid joint is presented in Table 6.

Table 6. Thermal effects on progressive failure of the joint

Torque [Nm]	T [°C]	F_{limit} [N]		F_{ult} [N]		Failure mode
		EXP	FEM	EXP	FEM	
0.5	+50	1438.4	1428.5	2097.7	2152.7	Bearing
0.5	-50	3304.2	3281.9	5226.2	5218.4	Shear-out

4.4 SHM method description

A common and useful method for structure health monitoring (SHM) uses the guided waves. The major advantage of these waves is the low energy losing while passing through the structure, which denotes an excellent energy transfer through the entire structure. The pioneer of this method is Horace Lamb who published his results for the first time in 1917 [29]. There are two types of propagation modes for these waves: symmetric (S_0, S_1…S_n) and anti-symmetric mode (A_0, A_1…A_n). In many of the applications, the most used modes for SHM testing are the fundamental mode S_0, which is dominating at 150-300 Hz and A_0 at 30-100 Hz frequencies. The reason for choosing these two fundamental modes is that they are easier to identify from the oscillation group of modes than the other superior ones. The SHM testing technique was used to experimentally observe the first ply failure in the laminate plate. The PWAS devices used in this experiment are produced by STEMiNC company, having the part number SMPL7W7T02412. They have a circular shape with 5 mm diameter and are presented in Fig. 15. The company code of the PWAS piezo-electric material is SM412 and the electro-mechanical properties are presented in Table 7, [30].

Figure 15. PWAS sensors positions on composite plate

Table 7. Electro-mechanical characteristics of the SM412 material, [30]

Property	Symbol	Value	Measurement unit
Electromechanical coupling coefficient	K_p	0.63	
	K_t	0.42	
	K_{31}	0.35	
Frequency constant	N_p	2080	Hz ● m
	N_t	2080	
	N_{31}	1560	
Piezoelectric constant	d_{33}	450	$\times 10^{-12}$m/v
	d_{31}	-190	
	g_{33}	25.6	$\times 10^{-3}$Vm/N
	g_{31}	-12.6	
Elastic Constant	Y_{33}	5.6	$\times 10^{10}$N/m^2
	Y_{11}	7.6	
Mechanical Quality Factor	Q_m	100	
Dielectric Constant	$\varepsilon T_{33/\varepsilon 0}$	1850	@1KHz
Dissipation Factor	tan δ	1.2	%@1KHz
Curie Temperature	T_c	320	°C
Density	r	7.8	g/cm^3

This type of input signal provides a gradual excitation with progressive amplitudes of the joint structure. The received signal is registered by connecting an oscilloscope probe on receiving PWAS. For also viewing the input signal, an oscilloscope probe is connected to the emitting PWAS. This signal is used as reference signal for data processing. All these probes are connected to an Agilent DSO-X 3034A digital storage oscilloscope, which performs the data acquisition. The entire process of data acquisition including the controll of the arbitrary wave form generator and the digital storage oscilloscope is performed by a Labview code running on a PC. This PC is connected to the other devices using USB and RS232C ports. Fig. 16 presents the damage initiation effect on the amplitude of the received signal and force-displacement characteristic curve, in order to be able to identify the first ply failure of the laminated plate of the joint. The amplitude curves represent the maximum (peak to peak) amplitudes of each receiving signals during the test. From the Fig. 16 it can be clearly seen that the amplitude of output signal is increasing with the joint stiffening up to the first lamina failure event. Afterwards the amplitude is decreasing due to the elastic properties degradation in the laminate plate on the post failure stage.

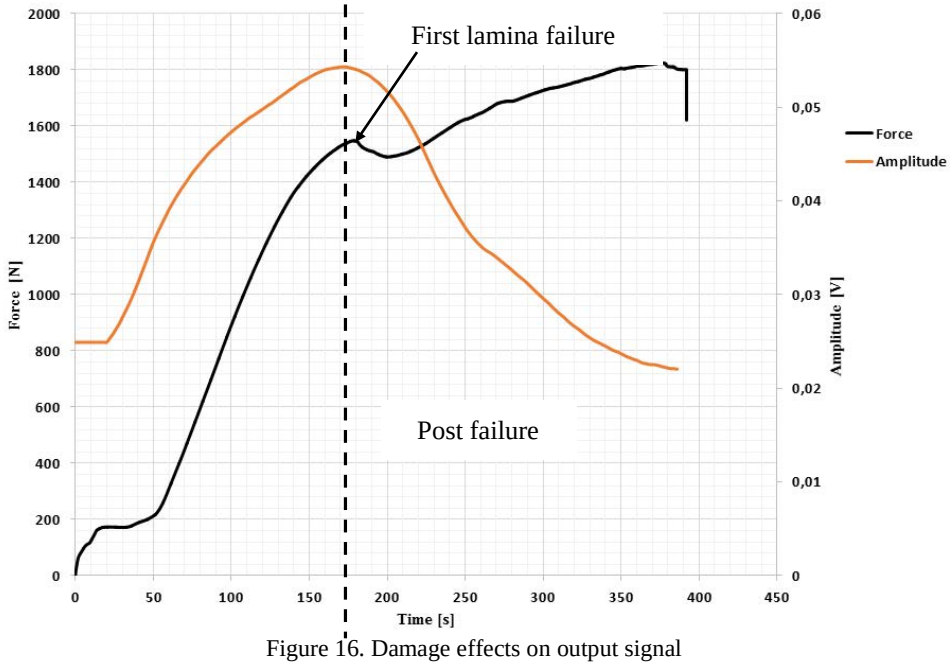

Figure 16. Damage effects on output signal

5. CONCLUSIONS

In this paper, the thermal effects on the stiffness, damage initiation and progressive failure for single-lap, single- bolt, hybrid metal-composite joints are investigated using both experimental technique and simulations with finite element method (FEM). Regarding the first ply failure (FPF) and strength evaluations, a progressive damage analysis (PDA) including nonlinear shear behavior of the ply, Hashin's failure criteria and strain-based continuous degradation rules was proposed. A 3D FEM model, which incorporates geometrical and contact full nonlinearities was developed in Patran as preprocessor and Nastran as explicit iterative solver. The PDA material model was implemented using a user-defined subroutine namely user_mat, using FOTRAN programming language. The simulation results were in good agreement with the experiments in terms of load-

displacement behavior, surface strains, joint stiffness, FPF and ultimate loads, which denoted that the 3D FEM model including full nonlinearities and explicit solver are quite accurate and can predict the metal-composite joint's mechanical behavior on both linear-elastic and nonlinear elastic ranges, including the failure modes as bearing, shear-out and net-section.

Regarding the thermal effects on the joint stiffness it can be seen from Table 4 that temperature decreases stiffness of the joint in the axial direction. The loading joint behavior released some interesting features at the beginning stage due to friction between the plates. This friction stage is composed of two parts: static and dynamic friction as can been seen from the load-displacement curves in Figs. 9 and 10. From these graphs it can be detected the friction load and, knowing the clamping force from torque level, therefore the friction coefficient between the plates can be calculated for the two temperatures study. Regarding the influence of temperature on the ultimate load of the joint, it has been observed that the load is decreasing while temperature is increasing, so as a global conclusion of the study, the temperature has reduced both the stiffness and strength of the joint. Therefore, it can be concluded that the SHM method accurately predict the first lamina failure and joint limit load which represents the fiber compression damage at the lamina level, because this local damage corresponds to a significant decreasing of the joint stiffness.

ACKNOWLEDGEMENTS

This article is an extension of the paper presented at ***International Conference of Aerospace Sciences "AEROSPATIAL 2018"***, 25 - 26 October 2018, Bucharest, Romania, (held at INCAS, B-dul Iuliu Maniu 220, sector 6), Section 4 – Materials and Structures.

REFERENCES

[1] Y. Xiao, T. Ishikawa, Bearing strength and failure behavior of bolted composite joints (part II: modeling and simulation), *Composites Science and Technology*, **65**, pp. 1032–1043, 2005.

[2] J. L. Chaboche, Continuum damage mechanics: part I – General concepts; part II – damage growth, crack initiation and crack Growth, *J Appl Mech*, **55**, pp.59–72, 1988.

[3] F. K. Chang, K. Y. Chang, Post-failure analysis of bolted composite joints in tension or shear-out mode failure, *J. Compos. Mater*., **21**, pp. 809–33, 1987.

[4] L. B. Lessard, M. M. Shokrieh, Two-dimensional modeling of composite pinned-joint failure, *J. Compos. Mater*., **29**, pp. 671–97, 1995.

[5] C. L. Hung, F. K. Chang, Bearing failure of bolted composite joints. Part II: model and verification, *J. Compos. Mater*., **30**, pp. 1359–400, 1996.

[6] S. J. Kim, J. S. Hwang, J. H. Kim, Progressive failure analysis of pin-loaded laminated composites using penalty finite element method, *AIAA J*., **36**(1), pp. 75–80, 1998.

[7] P. P.Camanho, F. L. Matthews, A progressive damage model for mechanically fastened joints in composite laminates, *J. Compos. Mater.*, **33**, pp. 2248–80, 1999.

[8] B. Okutan, The effects of geometric parameters on the failure strength for pin-loaded multi-directional fiber-glass reinforced epoxy laminate, *Compos. B. Eng.*, **33**(8), pp.567–8, 2002.

[9] K. I. Tserpes, G. Labeas, P. Papanikos, Th. Kermanidis, Strength prediction of bolted joints in graphite/epoxy composite laminates, *Compos. B. Eng.*, **33** (7), pp.521–9, 2002.

[10] Á. Olmedo, C., Santiuste On the prediction of bolted single-lap composite joints, *Compos. Struct.*, **94(6)**:2110–7, 2012.

[11] Z. Kapidz˘ic´, L. Nilsson, H. Ansell, Finite element modeling of mechanically fastened composite-aluminum joints in aircraft structures, *Compos. Struct.*, **109** (6), pp.198–210, 2014.

[12] A. K. Zerbst, G. Kuhlmann, C. Steenbock, et al., Progressive damage analysis of composite bolted joints with liquid shim layers using constant and continuous degradation models, *Compos. Struct*., **92** (2), pp.189–200, 2010.

[13] G. Kolks, K. I. Tserpes, Efficient progressive damage modeling of hybrid composite/titanium bolted joints. *Composites A*, **56** (1), pp.51–63, 2014.
[14] B. Egan, M. A. McCarthy, R. M. Frizzell, P. J. Gray, C. T. McCarthy, Modelling bearing failure in countersunk composite joints under quasi-static loading using 3D explicit finite element analysis, *Composite Structures*, **108**, pp. 963–977, 2014.
[15] A. Olmedo, C. Santiuste, E. Barbero, An analytical model for the secondary bending prediction in single-lap composite bolted-joints, *Composite Structures*, **111**, pp. 354–361, 2014.
[16] * * * ASTM D 5961, *Standard test method for bearing response of polymer matrix composite laminates*, 2007.
[17] * * * ASTM D 3039, *Standard Test Method for Tensile Properties of Polymer Matrix Composite Materials*, 2002.
[18] * * * Torayca T300 Technical Data Sheet No. CFA-001, Toray Carbon Fibers America Inc, www.torayusa.com
[19] * * * Derakane Momentum 411-350 Epoxy Venyl Ester Resin, Technical Data Sheet No. 1701 V3 F2, Ashland Inc, www.ashland.com
[20] * * * ECSS-E-HB-32-20 Part 2A, *Structural materials handbook - Part 2: Design calculation methods and general design aspects*, 2011.
[21] * * * MMPDS-05, *Metallic Materials Properties development and Standardization*, 2010.
[22] M. A. McCarthy, C. T. McCarthy, V. P. Lawlor, W. F. Stanley, Three-dimensional finite element analysis of single-bolt, single-lap composite bolted joints: part I - model development and validation, *Composite Structures*, **71**, pp.140–158, 2005.
[23] J. Schon, Coefficient of friction for aluminum in contact with a carbon fiber epoxy composite, *Tribol Int*, **37** (5), pp. 395–404, 2004.
[24] H. T. Hahn, S. W. Tsai, Nonlinear elastic behavior of unidirectional composite laminates, *Journal of Composite Materials*, **7** (1), pp.102–18, 1973.
[25] D. Ao, L. Yuqing, X. Haohui, Z. Yize, Progressive damage analysis of PFRP double-lap bolted joints using explicit finite element method, *Composite Structures*, **152**, pp. 860–869, 2016.
[26] Z. Hashin, Failure criteria for unidirectional fiber composites, *Journal of Applied Mechanics*, **47**, pp.329–34, 1980.
[27] Y. Zhou, H. Yazdani-Nezhad, M. A. Mccarthy, et al., A study of intra-laminar damage in double-lap, multi-bolt, composite joints with variable clearance using continuum damage mechanics, *Composite Structures*, **116** (9), pp. 441–52, 2014.
[28] R. M. O'Higgins, *An experimental and numerical study of damage initiation and growth in high strength glass and carbon fibre-reinforced composite materials* [PhD], University of Limerick, College of Engineering, 2007.
[29] H. Lamb, On waves in an elastic plate, *Proc. of the Royal Society, Mathematical, Physical and Engineering Sciences*, *93*, 1917, 114 – 128.
[30] *** http://www.steminc.com/piezo/PZ_property.asp.